ACS OMEGA

http://pubs.acs.org/journal/acsodf

Article

Intercalation of Nanoscale Multiferroic Spacers between the Two-Dimensional Interlayers of MXene

Bhargavi Koneru, Jhilmil Swapnalin, Srinivasan Natarajan, Adolfo Franco Jr, and Prasun Banerjee*

Cite This: *ACS Omega* 2022, 7, 20369−20375

Read Online

ACCESS | Metrics & More | Article Recommendations

ABSTRACT: We report a facile synthesis of MXene/bismuth ferrite ($Ti_3C_2T_x$ @ $BiFeO_3$) nanocomposites using hydrazine hydrate induced with the hydrothermal method. Preparation of the composite with hydrazine hydrate prevents the formation of $Bi_{25}FeO_{39}$ inside the matrix. The 25 wt % loading of $BiFeO_3$ acts as spacers for the multilayer restacking of MXene flakes by retaining the (002) plane. This promotes large dc conductivity with interfacial and defect dipole polarization mechanisms inside the composite material. The thinner M-H loop also indicates the minimal magnetic loss inside the composites. The facile synthesis strategy provides outstanding properties in $Ti_3C_2T_x$ @ $BiFeO_3$ composites as two-dimensional multiferroic materials.

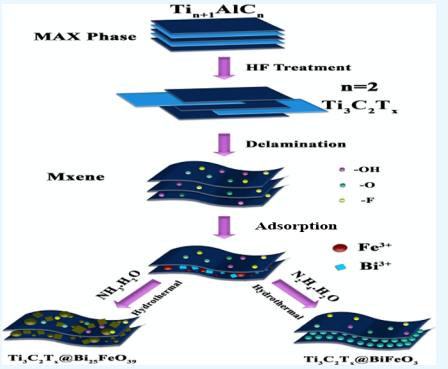

INTRODUCTION

The large-scale production of electric vehicles and wearable electronic devices is primarily integrated with the advanced technologies related to the efficient storage of electrical energies.[1,2] The higher cyclability and energy density make the electrochemical capacitors (ECs) reliable for such applications.[3] The charge storage mechanism and electrical properties of the electrode materials intrinsically determine the overall electrochemical properties of ECs.[4] Some materials with superior mechanical and electrical properties and the surface area largely control the EC's intrinsic electrode properties.[5−7] MXenes, one of the evolving 2D classes of materials offers all these electrochemical properties for the better performance of the EC.[8−10] The synthesis of MXenes is performed through selective etching techniques from the MAX phase ($M_{n+1}AX_n$).[11] Here, M is a transitional metal ion such as Ti, A is a group XIII element such as Al, X is a carbonitride/carbide/nitride, and n = 1, 2, or 3.[12] After the selective etching of the A layer, the MXene compositions are generally presented as $M_{n+1}X_nT_x$,[13] where T_x is the surface functional group such as F, O, OH, etc.

Very soon after discovering MXene, it grows to nearly 30 different compositions of transitional metal ions' carbonitrides/carbides/nitrides.[14] They mainly find applications in various fields of catalysis, water purification, sensors, optoelectronics, EMI shielding, and energy storage.[15−19] Among all these fields, the MXene family is mainly popular for energy storage applications.[20] Other than the properties such as superior mechanical and electrical properties and surface area, it also has functional groups and high conductivities.[21−23] So far, the use of MXene as an energy storage material for ECs reported higher capacitance.[24]

Generally, the conventional double-layer capacitors build electrical charge at the interface of the electrolytes and electrode materials. This process hindered the limit by which we could enhance the energy density of the capacitors. But the etching of the MAX powder leads to the formation of multilayers in MXene. Hence, integrating room-temperature multiferroics such as bismuth ferrite (BFO) as a spacer between the 2D MXene interlayers leads to a comprehensive capacitive charge storing mechanism.[25] In this mechanism, the presence of the dielectric bismuth ferrite material enhances the interaction of ions between the MXene layers, known as capacitive intercalations.[26] But so far, reported integration of BFO into $Ti_3C_2T_x$ MXene used solvothermal techniques with heavy agglomerations.[27] Hence, the effort to optimize the synthesis technique for $Ti_3C_2T_x$ @ $BiFeO_3$ using the facile hydrothermal method is still lagging.

Herein, we synthesized a $Ti_3C_2T_x$ @ $BiFeO_3$ composite with the hydrothermal technique. We chose hydrazine hydrate as a reducing agent because it helps intercalate the $BiFeO_3$ phase between the 2D layers of $Ti_3C_2T_x$. We further discuss the

Received: April 20, 2022
Accepted: May 25, 2022
Published: June 3, 2022

impact of replacing hydrazine hydrate with ammonia on the fabrication of the ferrite phase between the interlayers.

EXPERIMENTS

Materials. Ti_3AlC_2 (titanium aluminum carbide) was purchased from Nanochemazone. $Bi(NO_3)_3 \cdot 5H_2O$ (bismuth nitrate pentahydrate), $Fe(NO_3)_3 \cdot 9H_2O$ (iron nitrate nanohydrate), KOH (potassium hydroxide), $N_2H_4 \cdot H_2O$ (hydrazine hydrate), $NH_3 \cdot H_2O$ (ammonia), HNO_3 (nitric acid), HF (hydrofluoric acid), and C_2H_5OH (ethanol) were supplied by Alpha Chemika. No further purification methods were used after that.

Synthesis of MXene $Ti_3C_2T_x$. Initially, 4 g of MAX phase was slowly mixed with 200 mL of HF and kept in a polypyrrole container in a fume hood, avoiding any exothermic heating. After that, the mixture was kept at a temperature of 35°C for 72 h with gentle stirring with a polypyrrole rod at an interval of 12 h. The black powders were rinsed several times with demineralized water and finally washed with C_2H_5OH until they reached pH 6 using a centrifuge machine.

Synthesis of the Composites. In situ preparation of the $Ti_3C_2T_x$ @ $BiFeO_3$ composite was carried out by the hydrothermal technique. In general, 1.0244 g of $Bi(NO_3)_3 \cdot 5H_2O$ and 0.8533 g of $Fe(NO_3)_3 \cdot 9H_2O$ were dispersed into 20 mL of demineralized water with 4 M KOH until the pH reached 11. In another container, 1.54 g of $Ti_3C_2T_x$ powders were mixed with $N_2H_4 \cdot H_2O$ until the pH reached 11. Both the mixtures were transferred into a Teflon container slowly with continuous stirring. Finally, the hydrothermal reaction was carried out for 8 h at 220°C. Thereafter, the brown powders were cleaned with demineralized water and vacuum-desiccated for 12 h at a temperature of 60°C to obtain the $Ti_3C_2T_x$ @ $BiFeO_3$ composite. The same procedure was also followed for the $Ti_3C_2T_x$ @ $Bi_{25}FeO_{39}$ composite; only $N_2H_4 \cdot H_2O$ was replaced by $NH_3 \cdot H_2O$ in this case. For both cases, stoichiometric formulations were carried out to reach 25 wt % of ferrite phase loading within the MXene structure.

Composite Characterizations. X-ray diffraction (XRD) was performed with a Bruker D2 model diffractometer (CuKα, 1.5418 Å). The FTIR spectra were obtained from a spectrophotometer (PerkinElmer 2000) up to 4000 cm^{-1}. The morphology of the composite was determined with a Hitachi SU1510 scanning electron microscope. In diffuse reflection mode, the optical bandgap was deduced by a UV/Vis/NIR spectrometer (PerkinElmer Lambda 750). Magnetic measurements were taken at room temperature with a Quantum Design MPMS-XL EverCool SQUID for −16 kOe to 16 kOe field. The impedance and dielectric characteristics were found with a Hioki IM3536 LCR meter. The detailed process of the formation of the 2D structure and the integration of $BiFeO_3$ and $Bi_{25}FeO_{39}$ with $Ti_3C_2T_x$ is presented in Figure 1.

RESULTS AND DISCUSSION

XRD and Reaction Mechanism. The powder XRD profile of pure $BiFeO_3$, the composite $Ti_3C_2T_x$ @ $BiFeO_3$, the composite $Ti_3C_2T_x$ @ $Bi_{25}FeO_{39}$, MXene $Ti_3C_2T_x$, and pure Ti_3AlC_2 is shown in Figure 2. The HF etching completely removes the (104) plane reflection of Ti_3AlC_2 due to aluminum layers, as it completely disappears from the XRD profiles of $Ti_3C_2T_x$.[28] It also resulted in a broadening and leftward shift from 9.5° to 8.9° of the (002) plane peak due to

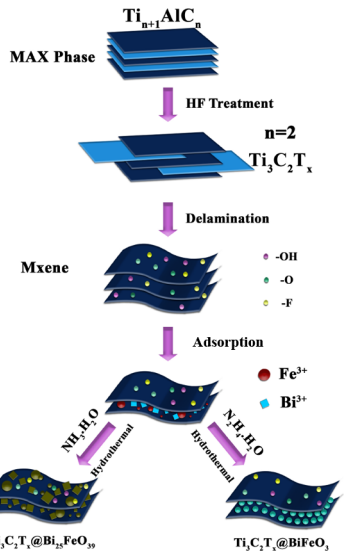

Figure 1. Demonstration of the fabrication process of the laminated structure and integration of the composite system (color online).

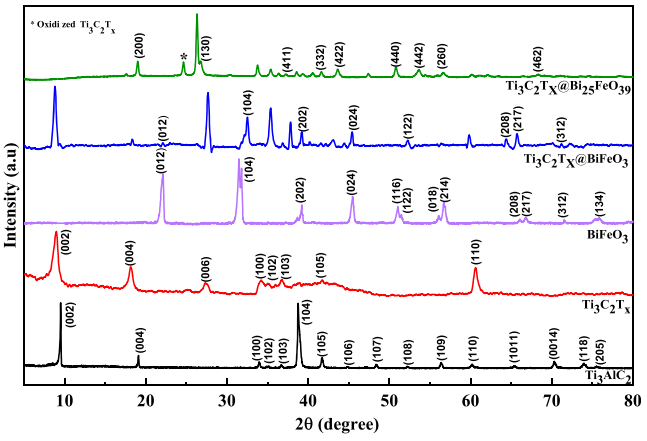

Figure 2. XRD for $Ti_3C_2T_x$ @ $Bi_{25}FeO_{39}$, the composite $Ti_3C_2T_x$ @ $BiFeO_3$, pure $BiFeO_3$, MXene $Ti_3C_2T_x$, and the Ti_3AlC_2 MAX phase (color online).

etching. The d spacing calculation with Bragg's law indicates the available spacing of 0.93 nm between the 2D layers of MXene.[29,30] The lattice constant a = 0.56 nm of $BiFeO_3$ corresponds to JCPDS 020-0169 with a rhombohedral $R3c$ space group of symmetries.[31] The retention of the (002) peak for $Ti_3C_2T_x$ @ $BiFeO_3$ indicates the successful interfacial interactions between the two materials. The higher intense peaks in the composite belong to $BiFeO_3$ in addition to $Ti_3C_2T_x$ peaks.[32] The characteristics peaks related to the $BiFeO_3$ phase appeared at (012), (104), (202), (024), (122), (208), (217), and (312). We may propose that hydrazine hydrate helps transfer the metal nitrates into metal hydroxide and oxide ions, which are then combined to form the $BiFeO_3$ phase:

$$Fe^{3+} + 6Bi^{3+} + 16OH^- \xrightarrow{N_2H_4 \cdot H_2O} Fe(OH)_4^- + Bi_6O_6^{6+} + 6H_2O \quad (1)$$

$$6Fe(OH)_4^- + Bi_6O_6^{6+} \rightarrow 6BiFeO_3 + 12H_2O \quad (2)$$

https://doi.org/10.1021/acsomega.2c02471
ACS Omega 2022, 7, 20369−20375

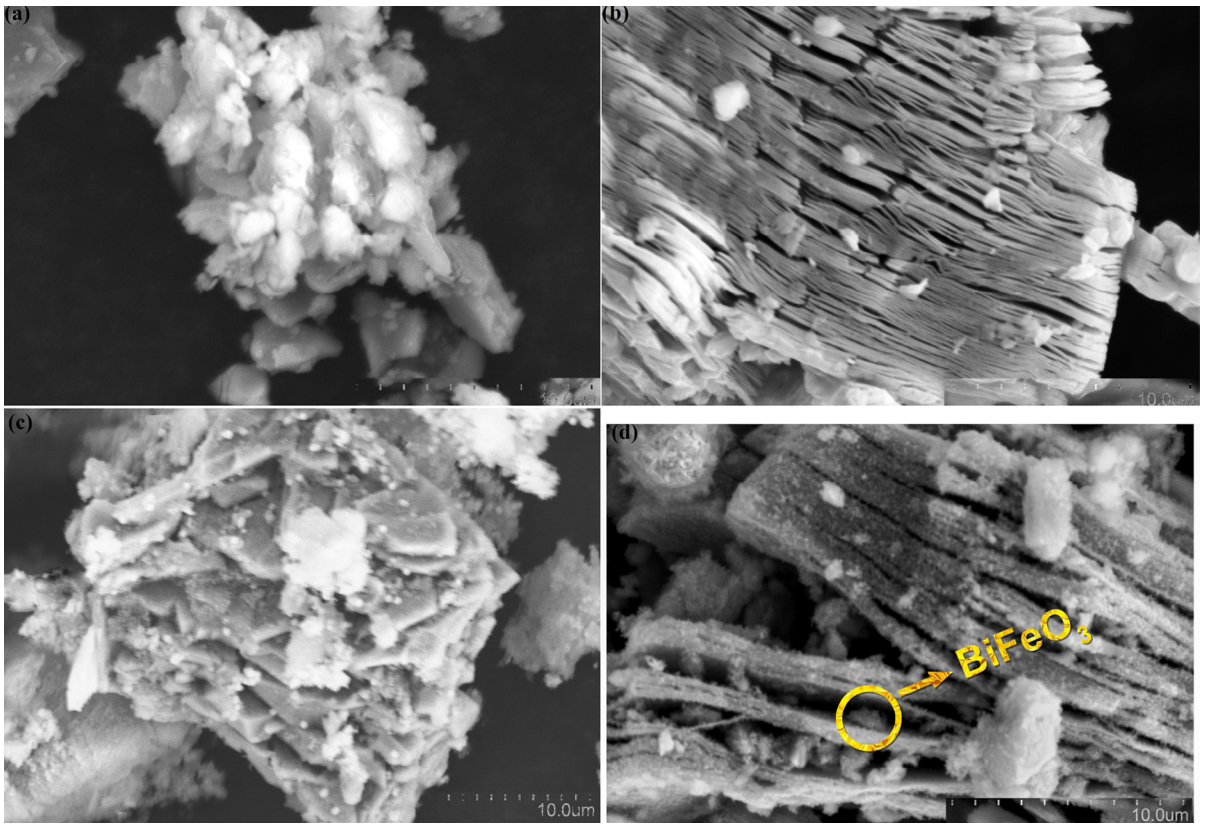

Figure 3. SEM micrographs for (a) Ti_3AlC_2, (b) $Ti_3C_2T_x$, (c) $Ti_3C_2T_x$ @ $Bi_{25}FeO_{39}$, and (d) $Ti_3C_2T_x$ @ $BiFeO_3$ composites.

On the contrary, the use of another reducing agent like ammonia may initiate a different mechanism for the integration of the metal hydroxide and oxide ions as:

$$6Fe(OH)_4^- + 25Bi_6O_6^{6+} + Ti_3C_2^{2+} + 146OH^- \xrightarrow{NH_3\cdot H_2O} 6Bi_{25}FeO_{39} + Ti_3C_2(OH)_2 + 84H_2O \quad (3)$$

This might result in unsuccessfully induced orientations of the $Bi_{25}FeO_{39}$ phase within the available d space of 0.93 nm, as its lattice constant is a = 1.02 nm for the cubic $I23$ space group (JCPDS 046-0416).[33] Hence, the characteristic (002) plane reflection completely disappears in the composite structures due to new interfacial interactions in the $Ti_3C_2T_x$ @ $Bi_{25}FeO_{39}$ composite. The gradual appearance of the $Ti_3C_2(OH)_2$ peaks at 25.5° was also noticed in the $Ti_3C_2T_x$ @ $Bi_{25}FeO_{39}$ composite.[34] The absence of the MXene peaks at 8.9° coming from (002) for the $Ti_3C_2T_x$ @ $Bi_{25}FeO_{39}$ composite indicates the aggregation of the $Bi_{25}FeO_{39}$ phase on the MXene flakes.[35]

SEM. Figure 3 presents micrographs obtained for all the samples. As can be noticed, the HF etching resulted in multilayer nanosheets of $Ti_3C_2T_x$ due to the removal of aluminum layers from the dense, compact structures of Ti_3AlC_2 shown in Figure 3b. The interlayer spacing in $Ti_3C_2T_x$ resulted in the (002) peak in the XRD profiles. The integration of $BiFeO_3$ retained the sheet structure of $Ti_3C_2T_x$, but it became thick and non-uniform as shown in Figure 3d. This may be the different orientation of the rhombohedral $BiFeO_3$ Bravais lattice in between the 2D MXene layers. But the use of ammonia while integrating the $Bi_{25}FeO_{39}$ phase in the $Ti_3C_2T_x$ structure resulted in the aggregation of the particles all around the 2D structures as shown in Figure 3c. Maybe that resulted in the absence of the (002) peak in the XRD profiles of $Ti_3C_2T_x$ @ $Bi_{25}FeO_{39}$ composites.[36]

FTIR Analysis. The vibrational spectra mainly originate from the hydroxyl group obtained from the FTIR characterization shown in Figure 4 for the $Ti_3C_2T_x$ @ $Bi_{25}FeO_{39}$ composite. The vibration (ν_{O-H}) from out-of-plane stretching and bending of the hydroxyl group originated at 3470 and 1695 m^{-1}, respectively.[37] The similar nature of the FTIR spectra between $Ti_3C_2T_x$ and $Ti_3C_2T_x$ @ $BiFeO_3$ indicates the absence of any oxidized phase in the composite structure.[38]

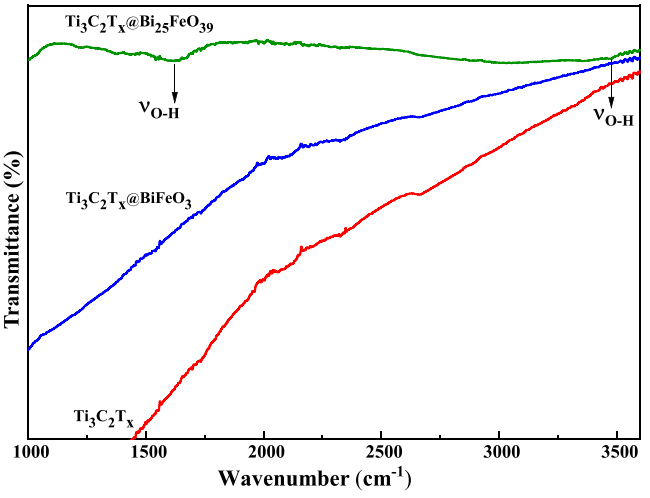

Figure 4. FTIR spectra for $Ti_3C_2T_x$, $Ti_3C_2T_x$ @ $BiFeO_3$, and $Ti_3C_2T_x$ @ $Bi_{25}FeO_{39}$ obtained through the hydrothermal reaction (color online).

https://doi.org/10.1021/acsomega.2c02471
ACS Omega 2022, 7, 20369−20375

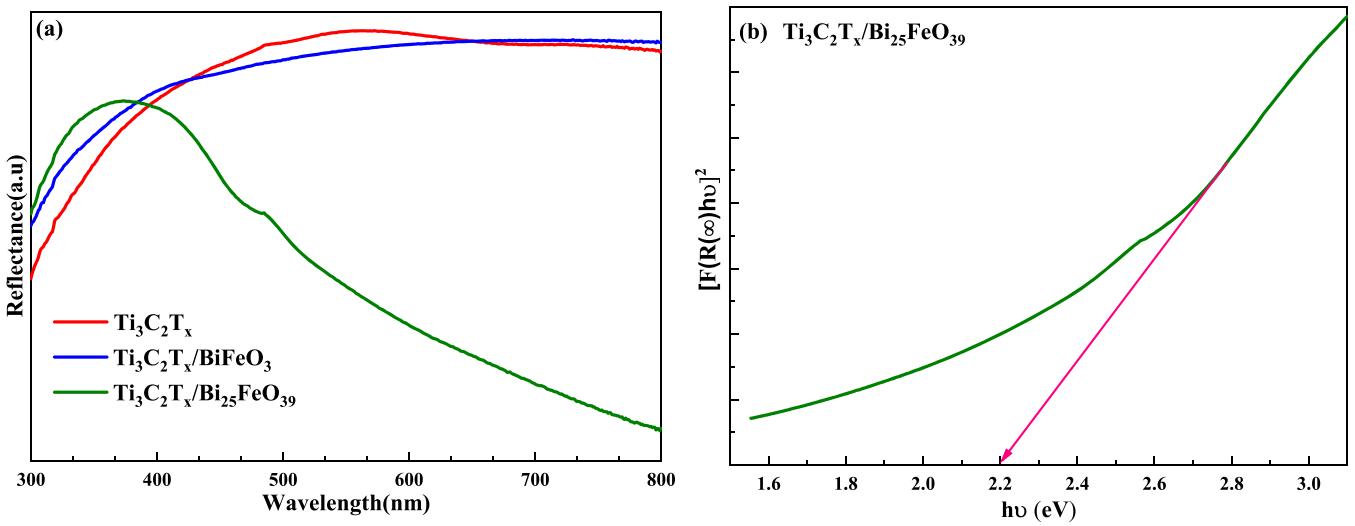

Figure 5. (a) Reflectance spectra of $Ti_3C_2T_x$, $Ti_3C_2T_x$ @ $BiFeO_3$, and $Ti_3C_2T_x$ @ $Bi_{25}FeO_{39}$ samples and (b) Tauc's plot of $Ti_3C_2T_x$ @ $Bi_{25}FeO_{39}$ (color online).

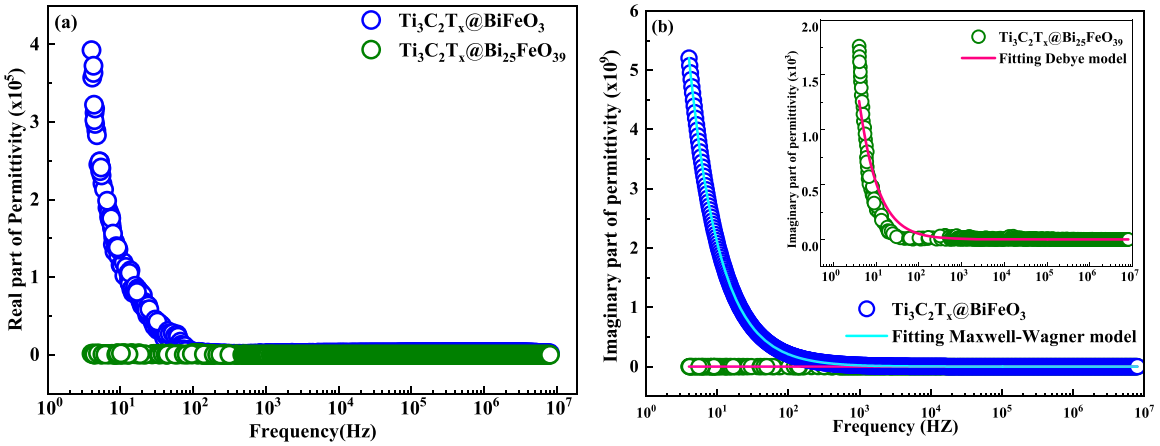

Figure 6. (a) Real part of permittivity with frequency for $Ti_3C_2T_x$ @ $BiFeO_3$ and $Ti_3C_2T_x$ @ $Bi_{25}FeO_{39}$ composites. (b) The dielectric data was fitted with the Maxwell–Wagner model. The pink line shows fitting results with the Debye model (color online).

Bandgap Studies. Bandgap determination was performed using the reflectance spectra shown in Figure 5a. The reflectance of light within the 3000–8000 Å range shows a continuous pattern for $Ti_3C_2T_x$ and $Ti_3C_2T_x$ @ $BiFeO_3$ samples, whereas the reflectance edge is visible for only $Ti_3C_2T_x$ @ $Bi_{25}FeO_{39}$. MXene has superior conductivity to metals. Hence, the possible overlapping of the conduction and valence bands resulted in a zero bandgap for MXene,[39] whereas the fabrication of $BiFeO_3$ with a small quantity retained the original multilayer sheet-like structure of MXene in the $Ti_3C_2T_x$ @ $BiFeO_3$ composite, which behaves similarly to the MXene powders. Not only that, the restacking in the $Ti_3C_2T_x$ @ $BiFeO_3$ composite does not affect the overall surface reflectance of the multilayer flakes.

The strong aggregation of the $Bi_{25}FeO_{39}$ particles strongly affects the interaction of the $Ti_3C_2T_x$ flakes with light, although the same 25 wt % anharmonic oscillations originating from the dipoles of the Fe, Bi, and O ions resulted in a separation between the two Morse curve states in $Ti_3C_2T_x$ @ $Bi_{25}FeO_{39}$ composites. The direct bandgap is determined by Tauc's plot with the Kubelka–Munk equation $E_g = h\nu - [F(R(\infty))h\nu]^2$ shown in Figure 5b.[40] The narrow bandgap energy for the $Ti_3C_2T_x$ @ $Bi_{25}FeO_{39}$ composites was determined to be 2.2 eV.

Capacitive and EIS Properties. The room-temperature variation of complex permittivity (ϵ' and ϵ'') with frequency is presented in Figure 6. The frequency dispersion due to 25 wt % ferrite phase loading on MXene can be observed for both the composites. But the higher value of the complex permittivity (ϵ' and ϵ'') was observed at lower frequencies for the $BiFeO_3$ phase fabrication on MXene. These directly indicate the better storage and dissipation capabilities of the electrical energies by the $Ti_3C_2T_x$ @ $BiFeO_3$ composites. The different dielectric properties between the two composites indicate a different dielectric relaxation mechanism within the composites.[41] This nature relates to the interfacial nature of the MXene sheets and the existence of the rhombohedral lattice structure of the $BiFeO_3$ nanoparticles. The interfacial nature of the MXene sheets resulted in the accumulation of electrons and ions in alternative layers, resulting in interfacial polarization. On the other hand, the rhombohedral lattice resulted in orientational relaxation inside the $Ti_3C_2T_x$ @ $BiFeO_3$ composites due to the spontaneous dipole moment with numerous defects in the $BiFeO_3$ crystals causing permanent defect dipoles.[42] These defect dipoles aligned themselves to the applied electric field when the frequencies were low, resulting in the orientational polarization. At higher frequency, due to the misalignment

https://doi.org/10.1021/acsomega.2c02471
ACS Omega 2022, 7, 20369–20375

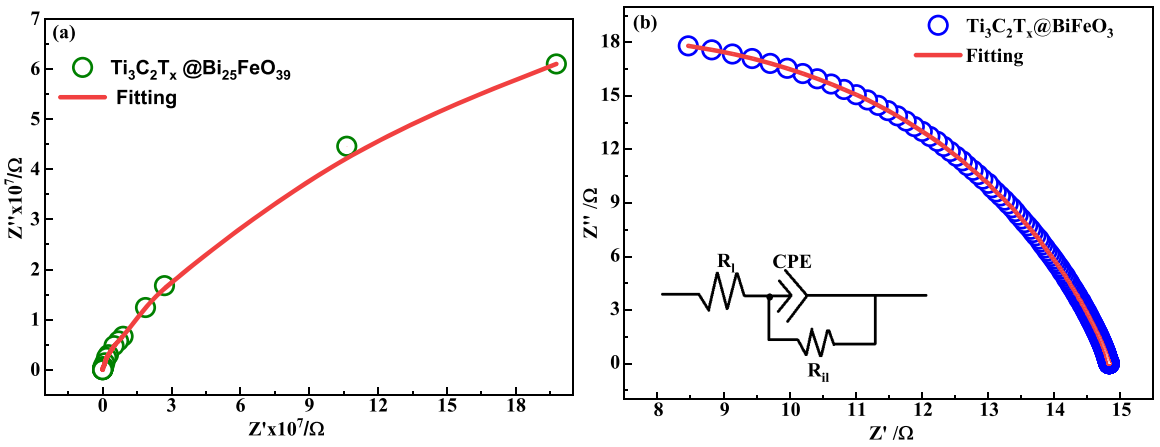

Figure 7. Nyquist plot of the (a) $Ti_3C_2T_x$ @ $Bi_{25}FeO_{39}$ and (b) $Ti_3C_2T_x$ @ $BiFeO_3$ composites with an equivalent circuit (inset) (color online).

owing to the effect of inertia, permittivity decreases. In general, the dielectric nature of the composites can be described by Debye and Maxwell−Wagner (M−W) mechanisms[43]

$$\varepsilon''(\omega) = \frac{\omega\tau(\varepsilon_s - \varepsilon_\infty)}{1 + \omega^2\tau^2}(\text{Debye}) \quad (4)$$

$$\varepsilon''(\omega) = \frac{(\varepsilon_s - \varepsilon_\infty)\omega\tau}{1 + \omega^2\tau^2} + \frac{\sigma}{\omega}(\text{M} - \text{W}) \quad (5)$$

whereas the first part of eq 5 is the same as the Debye mechanism of eq 4. The fitting of the dielectric data for both the composites is presented in Figure 6b. It can be visibly noticed that the $Ti_3C_2T_x$ @ $Bi_{25}FeO_{39}$ composites satisfy the Debye mechanism, whereas the $Ti_3C_2T_x$ @ $BiFeO_3$ composites obey the M−W mechanism. The dc conductivity (σ) determined from the fitting was found to be 1.30×10^{11} S/m $Ti_3C_2T_x$ @ $BiFeO_3$ composites. The strong agglomeration of the $Bi_{25}FeO_{39}$ phase affected the interfacial polarization due to the absence of the spontaneous dipole moments in the cubic lattice. These factors resulted in the Debye relaxation mechanism inside the $Ti_3C_2T_x$ @ $Bi_{25}FeO_{39}$ composites.

The resistance of the composites was further calculated using the Nyquist plots shown in Figure 7. A single semicircular half-arc with different radii was observed for the composites. The higher half-arc radius for the $Ti_3C_2T_x$ @ $Bi_{25}FeO_{39}$ composite indicates higher interface resistance, whereas the smaller half-arc radius of the $Ti_3C_2T_x$ @ $BiFeO_3$ composite indicates the easy charge transfer process between the interlayers.[44] Not only that, at higher frequencies, it offers the minimum real impedance and maximum imaginary impedance. The nature reverses with the decrease in frequency, indicating the capacitance behavior at room temperature.

This shift of the intra- and interlayer effects on the charge carriers can be understood with the equivalent circuit of the impedance data shown in the inset of Figure 7b, and the impedance of the circuit can be written as $R_l + R_{il}Z_{CPE}$, where R_l is the intralayer resistance, R_{il} is the interlayer resistance, and Z_{CPE} is the constant phase element. The obtained parameters with the fitting results are presented in Table 1. The interlayer resistance for the $Ti_3C_2T_x$ @ $Bi_{25}FeO_{39}$ composite was found to be in GΩ due to the agglomeration of the $Bi_{25}FeO_{39}$ phase, whereas the interlayer resistance for the $Ti_3C_2T_x$ @ $BiFeO_3$ composite is the same as that for the 2D $Ti_3C_2T_x$ as reported previously.[45] Hence, the successful fabrication of $BiFeO_3$ in the 2D $Ti_3C_2T_x$ resulted in a single relaxation mechanism, non-exponential variation, and decreased interlayer barrier on the mobility of charge carriers.

Table 1. Electrical Parameters Obtained from EIS Studies

parameter	$Ti_3C_2T_x$ @ $Bi_{25}FeO_{39}$	$Ti_3C_2T_x$ @ $BiFeO_3$
R_l (Ω)	44	45
R_{il} (Ω)	2.506×10^8	60
T (Ω s^{-1}) × 10^{-10}	6.654	1.130
p	0.70	0.99

Magnetic Properties. The magnetic hysteresis loop for the $Ti_3C_2T_x$ @ $Bi_{25}FeO_{39}$ and $Ti_3C_2T_x$ @ $BiFeO_3$ composites is presented in Figure 8 at room temperature with a maximum

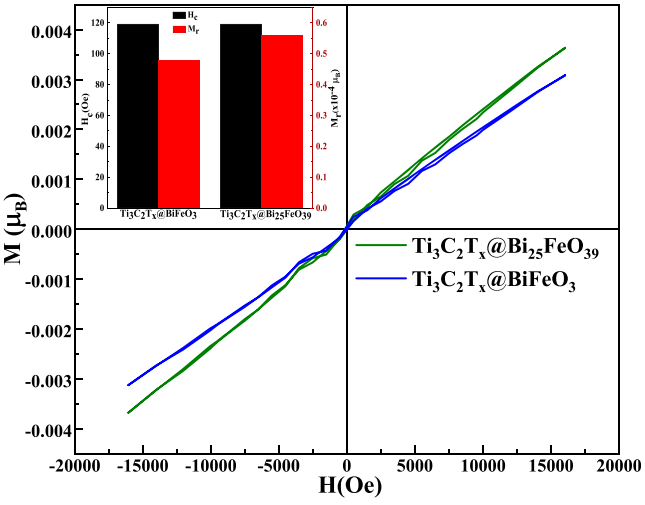

Figure 8. Room-temperature magnetic hysteresis loop for the $Ti_3C_2T_x$ @ $Bi_{25}FeO_{39}$ and $Ti_3C_2T_x$ @ $BiFeO_3$ composites. The inset shows the retentivity and coercivity of the composites (color online).

of 16,000 Oe of the applied magnetic field. It is evident from the graph that the composite shows a weak magnetic behavior and the maximum of 16,000 Oe field is not sufficient to saturate the magnetization. The magnetization in this regard is expressed with the formula $M = \frac{m \cdot M_s}{5585}$ in terms of Bohr magneton (μ_B).[46] The obtained values of the saturation magnetization (M_s) were 0.0036 and 0.0031 μ_B for the

https://doi.org/10.1021/acsomega.2c02471
ACS Omega 2022, 7, 20369−20375

$Ti_3C_2T_x$ @ $Bi_{25}FeO_{39}$ and $Ti_3C_2T_x$ @ $BiFeO_3$ composites with respect to the ferromagnetic element like iron with a value of 5 μ_B. Both the composites show an equal coercivity of 119 Oe, but the $Ti_3C_2T_x$ @ $Bi_{25}FeO_{39}$ composite has higher retentivity, as shown in the inset of Figure 8. Hence, a thinner M-H loop in $Ti_3C_2T_x$ @ $Bi_{25}FeO_{39}$ with retained weak magnetic behavior indicates a lower magnetic loss inside the composites.

CONCLUSIONS

The engineering of the 2D $Ti_3C_2T_x$ structures with interconnected multilayers with nanometer spacing is crucial for capacitor applications. The better electrical conductivity plays a vital role in the transport of electrons within this interconnected network of 2D layers. Hence, the hybridization of the multiferroic $BiFeO_3$ with spontaneous polarization due to the rhombohedral structure with MXene can be a critical step in fabricating superior capacitor materials. The main challenge associated with it is to stop agglomeration and provide mechanical support for the restacking of the flakes by finding a balance between the multiferroic spacers inside the 2D materials.

The design and synthesis of the composite material with an appropriate reducing agent and balanced wt % may lead to the desired morphology and performances using the electrostatic force of attraction of the ions. The use of ammonia as a reducing agent while hybridizing the multiferroic structure with the 2D $Ti_3C_2T_x$ structure using the hydrothermal method may lead to severe agglomeration with the $Ti_3C_2T_x$ @ $Bi_{25}FeO_{39}$ phase. The electrostatic interactions and neutralization of the −ve hydroxyl ion vibration by the +ve metal ions were observed with the redshift of the FTIR spectra with a 2.2 eV narrow bandgap energy in $Ti_3C_2T_x$ @ $Bi_{25}FeO_{39}$ agglomerated samples.

At the same time, the use of $N_2H_4 \cdot H_2O$ as a reducing agent while hybridizing the multiferroic structure with the 2D $Ti_3C_2T_x$ structure leads to a $Ti_3C_2T_x$ @ $BiFeO_3$ composite as a spacer between the multilayers. The fabrication of 25 wt % $BiFeO_3$ with MXene retained the original multilayer sheet-like structure and metallic behavior observed from SEM and UV−Vis analysis. The dielectric analysis indicates a dc conductivity of 1.30×10^{11} S/m magnitude with the presence of both interfacial and defect dipole polarization mechanisms. Moreover, the thin M-H loop means a minimal magnetic loss inside the composites. Hence, this straightforward, inexpensive, and quick method of preparation with superior properties may be applied to 2D multiferroic materials.

AUTHOR INFORMATION

Corresponding Author

Prasun Banerjee − *Multiferroic and Magnetic Material Research Laboratory, Gandhi Institute of Technology and Management (GITAM) University, Bengaluru, Karnataka 561203, India;* orcid.org/0000-0001-8473-6610; Email: pbanerje@gitam.edu

Authors

Bhargavi Koneru − *Multiferroic and Magnetic Material Research Laboratory, Gandhi Institute of Technology and Management (GITAM) University, Bengaluru, Karnataka 561203, India*

Jhilmil Swapnalin − *Multiferroic and Magnetic Material Research Laboratory, Gandhi Institute of Technology and Management (GITAM) University, Bengaluru, Karnataka 561203, India*

Srinivasan Natarajan − *Solid State and Structural Chemistry Unit, Indian Institute of Science, Bengaluru, Karnataka 560012, India*

Adolfo Franco Jr − *Instituto de Fisica, Universidade Federal de Goias, Goiania 74001-970, Brazil;* orcid.org/0000-0001-6428-6640

Complete contact information is available at: https://pubs.acs.org/10.1021/acsomega.2c02471

Notes

The authors declare no competing financial interest.

ACKNOWLEDGMENTS

P.B. and S.N. thank SERB, India, for the TARE fellowship and TAR/2021/000032 research grant. One of us (A.F.) is a recipient of 310440/2018-1 CNPq grant. B.K. and J.S. thank GITAM University for the Dr. M. V. V. S. Murthi and T. A. research fellowship.

REFERENCES

(1) Huang, Q.; Wang, D.; Zheng, Z. Textile-based electrochemical energy storage devices. *Adv. Energy Mater.* **2016**, *6*, 1600783.

(2) Chang, J.; Jin, M.; Yao, F.; Kim, T. H.; Le, V. T.; Yue, H.; Gunes, F.; Li, B.; Ghosh, A.; Xie, S.; Lee, Y. H. Asymmetric supercapacitors based on graphene/MnO2 nanospheres and graphene/MoO3 nanosheets with high energy density. *Adv. Funct. Mater.* **2013**, *23*, 5074−5083.

(3) Beidaghi, M.; Gogotsi, Y. Capacitive energy storage in micro-scale devices: recent advances in design and fabrication of micro-supercapacitors. *Energy Environ. Sci.* **2014**, *7*, 867−884.

(4) Mendoza-Sánchez, B.; Gogotsi, Y. Synthesis of two-dimensional materials for capacitive energy storage. *Adv. Mater.* **2016**, *28*, 6104−6135.

(5) Tian, W.; VahidMohammadi, A.; Wang, Z.; Ouyang, L.; Beidaghi, M.; Hamedi, M. M. Layer-by-layer self-assembly of pillared two-dimensional multilayers. *Nat. Commun.* **2019**, *10*, 1−10.

(6) Lu, X.; Zhu, J.; Wu, W.; Zhang, B. Hierarchical architecture of PANI@ TiO2/Ti3C2Tx ternary composite electrode for enhanced electrochemical performance. *Electrochim. Acta* **2017**, *228*, 282−289.

(7) Hu, Y.; Guan, C.; Feng, G.; Ke, Q.; Huang, X.; Wang, J. Flexible Asymmetric Supercapacitor Based on Structure-Optimized Mn3O4/Reduced Graphene Oxide Nanohybrid Paper with High Energy and Power Density. *Adv. Funct. Mater.* **2015**, *25*, 7291−7299.

(8) Wang, Q. H.; Kalantar-Zadeh, K.; Kis, A.; Coleman, J. N.; Strano, M. S. Electronics and optoelectronics of two-dimensional transition metal dichalcogenides. *Nat. Nanotechnol.* **2012**, *7*, 699−712.

(9) Anasori, B.; Lukatskaya, M. R.; Gogotsi, Y. 2D metal carbides and nitrides (MXenes) for energy storage. *Nat. Rev. Mater.* **2017**, *2*, 1−17.

(10) Tan, C.; Cao, X.; Wu, X.-J.; He, Q.; Yang, J.; Zhang, X.; Chen, J.; Zhao, W.; Han, S.; Nam, G.-H.; et al. Recent advances in ultrathin two-dimensional nanomaterials. *Chem. Rev.* **2017**, *117*, 6225−6331.

(11) Mashtalir, O.; Naguib, M.; Mochalin, V. N.; Dall Agnese, Y.; Heon, M.; Barsoum, M. W.; Gogotsi, Y. Intercalation and delamination of layered carbides and carbonitrides. *Nat. Commun.* **2013**, *4*, 1−7.

(12) Chen, B.; Song, Q.; Zhou, Z.; Lu, C. A novel sandwiched porous MXene/polyaniline nanofibers composite film for high capacitance supercapacitor electrode. *Adv. Mater. Interfaces* **2021**, *8*, 2002168.

(13) Boota, M.; Pasini, M.; Galeotti, F.; Porzio, W.; Zhao, M.-Q.; Halim, J.; Gogotsi, Y. Interaction of polar and nonpolar polyfluorenes with layers of two-dimensional titanium carbide (MXene):

intercalation and pseudocapacitance. *Chem. Mater.* **2017**, *29*, 2731−2738.
(14) Urbankowski, P.; Anasori, B.; Makaryan, T.; Er, D.; Kota, S.; Walsh, P. L.; Zhao, M.; Shenoy, V. B.; Barsoum, M. W.; Gogotsi, Y. Synthesis of two-dimensional titanium nitride Ti4N3 (MXene). *Nanoscale* **2016**, *8*, 11385−11391.
(15) Guo, Z.; Zhou, J.; Zhu, L.; Sun, Z. MXene: a promising photocatalyst for water splitting. *J. Mater. Chem. A* **2016**, *4*, 11446−11452.
(16) Geng, D.; Zhao, X.; Chen, Z.; Sun, W.; Fu, W.; Chen, J.; Liu, W.; Zhou, W.; Loh, K. P. Direct synthesis of large-area 2D Mo2C on in situ grown graphene. *Adv. Mater.* **2017**, *29*, 1700072.
(17) Gao, G.; O'Mullane, A. P.; Du, A. 2D MXenes: a new family of promising catalysts for the hydrogen evolution reaction. *ACS Catal.* **2017**, *7*, 494−500.
(18) Lukatskaya, M. R.; Mashtalir, O.; Ren, C. E.; Dall Agnese, Y.; Rozier, P.; Taberna, P. L.; Naguib, M.; Simon, P.; Barsoum, M. W.; Gogotsi, Y. Cation intercalation and high volumetric capacitance of two-dimensional titanium carbide. *Science* **2013**, *341*, 1502−1505.
(19) Lukatskaya, M. R.; Kota, S.; Lin, Z.; Zhao, M.-Q.; Shpigel, N.; Levi, M. D.; Halim, J.; Taberna, P.-L.; Barsoum, M. W.; Simon, P.; et al. Ultra-high-rate pseudocapacitive energy storage in two-dimensional transition metal carbides. *Nat. Energy* **2017**, *2*, 1−6.
(20) VahidMohammadi, A.; Moncada, J.; Chen, H.; Kayali, E.; Orangi, J.; Carrero, C. A.; Beidaghi, M. Thick and freestanding MXene/PANI pseudocapacitive electrodes with ultrahigh specific capacitance. *J. Mater. Chem. A* **2018**, *6*, 22123−22133.
(21) He, P.; Liu, Z.-Y.; Mao, G.-B.; Liu, Q.; Zheng, M.-J.; Zuo, R.-Z.; Cao, W.-Q.; Hou, Z.-L.; Yuan, J.; Cao, M.-S. MXene films: toward high-performance electromagnetic interference shielding and supercapacitor electrode. *Composites, Part A* **2022**, No. 106935.
(22) Zhang, M.; Yang, H.-J.; Li, Y.; Cao, W.-Q.; Fang, X.-Y.; Yuan, J.; Cao, M.-S. Cobalt doping of bismuth ferrite for matched dielectric and magnetic loss. *Appl. Phys. Lett.* **2019**, *115*, 212902.
(23) Wang, X.-X.; Zhang, M.; Shu, J.-C.; Wen, B.; Cao, W.-Q.; Cao, M.-S. Thermally tailoring dielectric genes in graphene-based heterostructure to manipulate electromagnetic response. *Carbon* **2021**, *184*, 136−145.
(24) Kayali, E.; VahidMohammadi, A.; Orangi, J.; Beidaghi, M. Controlling the dimensions of 2D MXenes for ultrahigh-rate pseudocapacitive energy storage. *ACS Appl. Mater. Interfaces* **2018**, *10*, 25949−25954.
(25) Alsafari, I. A.; Munir, S.; Zulfiqar, S.; Saif, M. S.; Warsi, M. F.; Shahid, M. Synthesis, characterization, photocatalytic and antibacterial properties of copper Ferrite/MXene (CuFe2O4/Ti3C2) nanohybrids. *Ceram. Int.* **2021**, *47*, 28874−28883.
(26) Xie, Y.; Naguib, M.; Mochalin, V. N.; Barsoum, M. W.; Gogotsi, Y.; Yu, X.; Nam, K.-W.; Yang, X.-Q.; Kolesnikov, A. I.; Kent, P. R. Role of surface structure on Li-ion energy storage capacity of two-dimensional transition-metal carbides. *J. Am. Chem. Soc.* **2014**, *136*, 6385−6394.
(27) Iqbal, M. A.; Tariq, A.; Zaheer, A.; Gul, S.; Ali, S. I.; Iqbal, M. Z.; Akinwande, D.; Rizwan, S. Ti3C2-MXene/bismuth ferrite nanohybrids for efficient degradation of organic dyes and colorless pollutants. *ACS Omega* **2019**, *4*, 20530−20539.
(28) Liu, X.; Chen, C. Mxene enhanced the photocatalytic activity of ZnO nanorods under visible light. *Mater. Lett.* **2020**, *261*, No. 127127.
(29) Li, Z.; Wang, L.; Sun, D.; Zhang, Y.; Liu, B.; Hu, Q.; Zhou, A. Synthesis and thermal stability of two-dimensional carbide MXene Ti3C2. *Mater. Sci. Eng., B* **2015**, *191*, 33−40.
(30) Gao, L.; Chen, H.; Kuklin, A. V.; Wageh, S.; Al-Ghamdi, A. A.; Agren, H.; Zhang, H. Optical Properties of Few-Layer Ti3CN MXene: From Experimental Observations to Theoretical Calculations. *ACS Nano* **2022**, 3059.
(31) Verma, R.; Chauhan, A.; Batoo, K. M.; Kumar, R.; Hadhi, M.; Raslan, E. H.; et al. Effect of calcination temperature on structural and morphological properties of bismuth ferrite nanoparticles. *Ceram. Int.* **2021**, *47*, 3680−3691.
(32) Banerjee, P.; Franco, A., Jr. Enhanced dielectric and magnetic properties in multiferroic Bi0. 99Y0. 01Fe0. 99Ni0. 01O3 ceramic. *Mater. Lett.* **2016**, *184*, 17−20.
(33) Scurti, C. A.; Auvray, N.; Lufaso, M. W.; Takeda, S.; Kohno, H.; Arenas, D. J. Electron diffraction study of the sillenites Bi12SiO20, Bi25FeO39 and Bi25InO39: Evidence of short-range ordering of oxygen-vacancies in the trivalent sillenites. *AIP Adv.* **2014**, *4*, No. 087125.
(34) Qing, Y.; Zhou, W.; Luo, F.; Zhu, D. Titanium carbide (MXene) nanosheets as promising microwave absorbers. *Ceram. Int.* **2016**, *42*, 16412−16416.
(35) He, P.; Wang, X.-X.; Cai, Y.-Z.; Shu, J.-C.; Zhao, Q.-L.; Yuan, J.; Cao, M.-S. Tailoring Ti3C2T x nanosheets to tune local conductive network as an environmentally friendly material for highly efficient electromagnetic interference shielding. *Nanoscale* **2019**, *11*, 6080−6088.
(36) Xiong, D.; Li, X.; Bai, Z.; Lu, S. Recent advances in layered Ti3C2Tx MXene for electrochemical energy storage. *Small* **2018**, *14*, 1703419.
(37) Djire, A.; Bos, A.; Liu, J.; Zhang, H.; Miller, E. M.; Neale, N. R. Pseudocapacitive Storage in Nanolayered Ti2NT x MXene Using Mg-Ion Electrolyte. *ACS Appl. Nano Mater.* **2019**, *2*, 2785−2795.
(38) Shi, L.; Xu, C.; Jiang, D.; Sun, X.; Wang, X.; Wang, Q.; Zhang, Y.; Qu, X.; Du, F. Enhanced interaction in TiO2/BiVO4 heterostructures via MXene Ti3C2-derived 2D-carbon for highly efficient visible-light photocatalysis. *Nanotechnology* **2019**, *30*, No. 075601.
(39) Han, X.; An, L.; Hu, Y.; Li, Y.; Hou, C.; Wang, H.; Zhang, Q. Ti3C2 MXene-derived carbon-doped TiO2 coupled with g-C3N4 as the visible-light photocatalysts for photocatalytic H2 generation. *Appl. Catal., B* **2020**, *265*, No. 118539.
(40) Pessoni, H. V.; Alves, T. E.; Banerjee, P.; Junior, A. F. Functional properties of Ho3+ substituted cobalt ferrite in the context of the reduced mass model. *Phys. B* **2019**, *575*, No. 411676.
(41) Franco, A.; Banerjee, P.; Lima, R. Dielectric and magnetic properties of three-layers laminated ceramic composite, K 0.5 Na 0.5 NbO 3/CoFe 2 O 4/K 0.5 Na 0.5 NbO 3. *J. Mater. Sci.: Mater. Electron.* **2018**, *29*, 4357−4364.
(42) de Lira, S. O.; E Silva, R. L. D. S.; Banerjee, P.; Franco, A., Jr. Effects of defect dipoles on the colossal permittivity of ambipolar co-doped rutile TiO2 ceramics. *J. Phys. Chem. Solids* **2020**, *143*, No. 109456.
(43) Banerjee, P.; Franco, A., Jr. Substitution-induced near phase transition with Maxwell−Wagner polarization in SrBi2 (Nb1- xAx) 2O9 ceramics [A= W, Mo and x= 0, 0.025]. *Phys. Status Solidi A* **2017**, *214*, 1700067.
(44) Miranda, G. G.; E'Silva, R. L. D. S.; Banerjee, P.; Franco, A., Jr. Role of Ga presence into the heterojunction of metal oxide semiconductor on the stability and tunability ZnO ceramics. *Ceram. Int.* **2020**, *46*, 23390−23396.
(45) Khadidja, M. F.; Fan, J.; Li, S.; Li, S.; Cui, K.; Wu, J.; Zeng, W.; Wei, H.; Jin, H.-G.; Naik, N.; et al. Hierarchical ZnO/MXene composites and their photocatalytic performances. *Colloids Surf., A* **2021**, *628*, No. 127230.
(46) Ratkovski, D. R.; Ribeiro, P. R. T.; Machado, F. L. A.; Banerjee, P.; Franco, A., Jr. On the magnetic properties of the multiferroic ceramics Bi0. 99Y0. 01Fe1-xNixO3. *J. Magn. Magn. Mater.* **2018**, *451*, 620−624.

https://doi.org/10.1021/acsomega.2c02471
ACS Omega 2022, 7, 20369−20375